water

MDPI

Article

# Integration of Remote Sensing Evapotranspiration into Multi-Objective Calibration of Distributed Hydrology–Soil–Vegetation Model (DHSVM) in a Humid Region of China

**Suli Pan, Li Liu, Zhixu Bai and Yue-Ping Xu ***

Institute of Hydrology and Water Resources, College of Civil Engineering and Architecture, Zhejiang University, Hangzhou 310058, China; pansuli@zju.edu.cn (S.P.); li_liu@zju.edu.cn (L.L.); zhixu_bai@zju.edu.cn (Z.B.)
* Correspondence: yuepingxu@zju.edu.cn

Received: 5 November 2018; Accepted: 10 December 2018; Published: 12 December 2018


**Abstract:** This study presents an approach that integrates remote sensing evapotranspiration into multi-objective calibration (i.e., runoff and evapotranspiration) of a fully distributed hydrological model, namely a distributed hydrology–soil–vegetation model (DHSVM). Because of the lack of a calibration module in the DHSVM, a multi-objective calibration module using ε-dominance non-dominated sorted genetic algorithm II (ε-NSGAII) and based on parallel computing of a Linux cluster for the DHSVM (εP-DHSVM) is developed. The module with DHSVM is applied to a humid river basin located in the mid-west of Zhejiang Province, east China. The results show that runoff is simulated well in single objective calibration, whereas evapotranspiration is not. By considering more variables in multi-objective calibration, DHSVM provides more reasonable simulation for both runoff (*NS*: 0.74% and *PBIAS*: 10.5%) and evapotranspiration (*NS*: 0.76% and *PBIAS*: 8.6%) and great reduction of equifinality, which illustrates the effect of remote sensing evapotranspiration integration in the calibration of hydrological models.

**Keywords:** remote sensing evapotranspiration; multi-objective calibration; εP-DHSVM; MODIS; SEBAL

## 1. Introduction

Parameter values of hydrological models must be evaluated through calibration to match the model response to historical observed data [1–4]. Model calibration is usually based on the comparison of observed and simulated runoff at a limited number of stations [1]. Considering the multiple processes and numerous parameters in distributed hydrological models, this approach is not very effective and often leads to parameter equifinality problems [5]. Moreover, calibration with single model objective (that is to say, runoff) is unlikely to optimize other model outputs (such as evapotranspiration and soil moisture) owing to the underlying principle in distributed hydrological models. The application of multi-objective calibration in distributed hydrological models can optimize multiple model outputs simultaneously and therefore reduce possible equifinality problems [6].

Evapotranspiration is the key element in the hydrologic cycle and has an important impact on agricultural management and water resources [7,8]. However, the observation of evapotranspiration is often more difficult than other variables, such as runoff and precipitation. Observed evapotranspiration from hydrological stations is measured by evaporation pans, which can represent potential evapotranspiration but not actual evapotranspiration [9]. Remote sensing data provide an alternative solution for this problem. Over the past decades, remote sensing data have been widely used for precipitation estimation, land use classification, evapotranspiration inversion, vegetation indices and soil moisture prediction [10–17]. For ungauged basins, remote sensing data are particularly useful

in drought forecasting, runoff estimation and rainfall frequency analysis [18–23]. Zhang et al. [17] adopted a leaf area index (LAI) product from a moderate resolution imaging spectrometer (MODIS) to derive evapotranspiration at an eight-day scale. Rajib et al. [5] applied remote sensing soil moisture, together with observed runoff, to calibrate a soil and water assessment tool (SWAT) model. Previous studies employing remote sensing data includes many fields [24–30]. However, less work has been done in integration of remote sensing evapotranspiration into multi-objective calibration of a fully distributed hydrological model.

There are various remote sensing-based models for evapotranspiration estimation [31], including the surface energy balance system (SEBS) [32], the surface energy balance algorithm for land (SEBAL) [33], the two-source energy balance model (TSEB) [34–36] and mapping evapotranspiration at high resolution with internalized calibration (METRIC) [37]. Of these models, SEBAL can map evapotranspiration with minimum ground-based data [38]. Moreover, the SEBAL model has been successfully applied to derive evapotranspiration under different climatic conditions at both field and catchment scales in more than 30 countries around the world, and it was found that the accuracy of derived evapotranspiration at the field scale was 85% and 95% at daily and seasonal time scales, respectively [39–41].

Multi-objective automatic calibration can reduce equifinality in parameter selection and overcome the disadvantages of manual calibration. However, the demand in terms of computation time is quite onerous [42]. Therefore, parallel computing is applied for multi-objective calibration in this study. For multi-objective evolutionary algorithms, genetic algorithms (GAs) [43,44] have drawn increasing attention and have been successfully applied to multi-objective problems in many fields, including hydrological modelling. Kollat and Reed [45] proposed ε-domination non-dominated sorting genetic algorithm II (ε-NSGAII), based on non-dominated sorting genetic algorithm II (NSGAII) and ε domination archiving. Kollat and Reed [46] compared the performances of four multi-objective algorithms, and the result revealed that ε-NSGAII is efficient, reliable and easy-to-use. In addition, the application of ε domination, adaptive population sizing, and self-termination in ε-NSGAII minimizes the population need for searching for an optimal solution. To compensate for a lack of calibration module in the distributed hydrology–soil–vegetation model (DHSVM) [7,47], a multi-objective calibration module using the ε-dominance non-dominated sorted genetic algorithm II (ε-NSGAII) and based on parallel computing of a Linux cluster for the DHSVM (εP-DHSVM) is developed in this study.

The motivation of this study is to explore the effect of integrating remote sensing evapotranspiration into multi-objective calibration on model performance of runoff and evapotranspiration simulation based on the DHSVM. Moreover, it is worthwhile to investigate the feasibility of deriving long time-series of evapotranspiration from MODIS via the SEBAL method. As far as the authors know, development of an auto-calibration module for the DHSVM is rare. This study is carried out for a humid region of China, namely, the Jinhua River Basin. Hence, the objectives of this study are to: (1) estimate actual evapotranspiration at a daily time scale based on MODIS and meteorological data via the SEBAL model; (2) develop a multi-objective calibration module (ε-NSGAII) based on parallel computing of a Linux cluster for the DHSVM (εP-DHSVM); (3) assess performance of evapotranspiration simulation when the DHSVM model is calibrated with single objective (runoff); and, (4) integrate remote sensing actual evapotranspiration into multi-objective calibration of the DHSVM and evaluate how runoff and evapotranspiration simulation are affected.

## 2. Study Area

The Jinhua River Basin is located in the mid-west of Zhejiang Province, east China (Figure 1a). The length of this river is 195 km and its catchment area above the Jinhua hydrological station is 5996 km$^2$. The study area is subject to an Asian monsoon climate, and precipitation is strongly summer-dominant, occurring mostly from May to September. Based on fifty years (1962–2011) of meteorological data, the mean annual precipitation in Jinhua River Basin is 1404.9 mm. As shown in Figure 1c, the elevation ranges from 29 to 1296 m, and most areas of this watershed are located at low

altitudes. The average air temperature is about 17 °C, and the maximum air temperature is more than 40 °C. Soils are mainly clay loam, sandy loam and loam, with percentages of 55.4%, 16.5% and 15.8%, respectively. The land use types of the study area are primarily croplands, mixed forest and grasslands, with percentages of 36.7%, 29.6% and 22.9%, respectively. Figure 1 shows the location, elevation of the study area (digital elevation model, DEM), and hydro-meteorological stations used in this study.

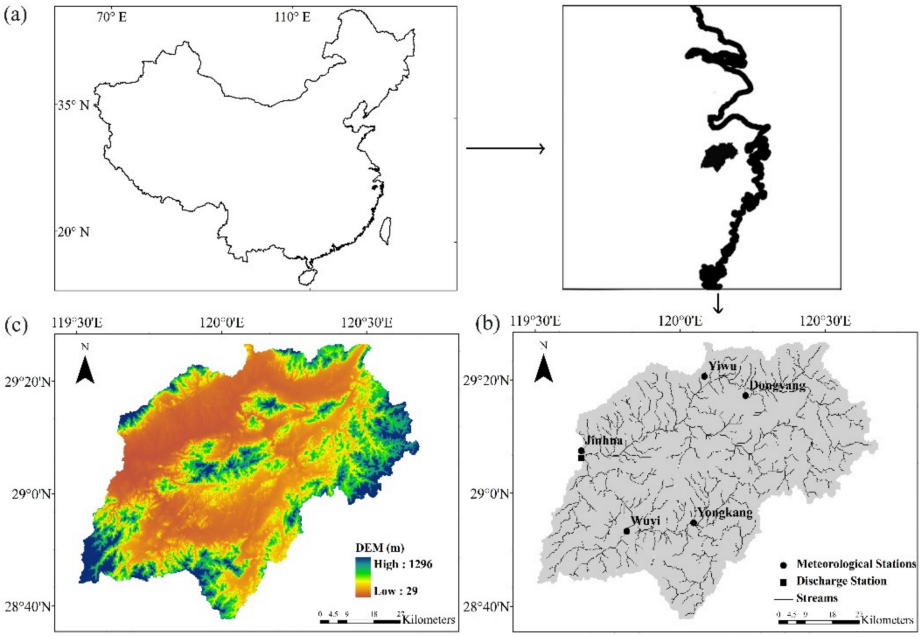


**Figure 1.** (**a**) Location of study area, (**b**) hydro-meteorological stations and (**c**) digital elevation model (DEM) used in the study.

## 3. Data and Methods

### *3.1. Experiment Design*

The general framework of this study is presented in Figure 2. In a previous study by the authors [48], a two-step sensitivity analysis method was coupled to the DHSVM, owing to the lack of sensitivity analysis module in the hydrological model. A global sensitivity analysis method (ANOVA) was adopted in the first step of sensitivity analysis to obtain preliminary sensitive parameters in the hydrological model. In the second step, final sensitivity parameters and their interactions could be obtained through a more sophisticated global sensitivity analysis method called Sobol's sensitivity analysis. These final sensitivity parameters were then used in model calibration in this study. Sobol's sensitivity analysis method is a variance-based method, which can measure the contribution of a single parameter to model outputs and its interactions with others. The criteria for determining sensitivity of parameters in Sobol's method are sensitivity indices, including first order, second order and total order indices [49,50]. The first order sensitivity index measures the main effect of single parameter, while the second order sensitivity index measures the interaction effect between two parameters. The total order sensitivity index measures the main effect of single parameter and interactions with other parameters, indicating that the difference between total order and first order sensitivity indices measures the interactions of one parameter with others. All details about the first part of this framework (Box I, Figure 2) can be found in [48].

Box II (Figure 2) shows the main methods used in the present study. In multi-objective calibration, remote sensing evapotranspiration derived from MODIS data via SEBAL is used as the observation data. Moreover, the performance of simulating runoff and evapotranspiration in multi-objective calibration after remote sensing evapotranspiration integration will be evaluated.

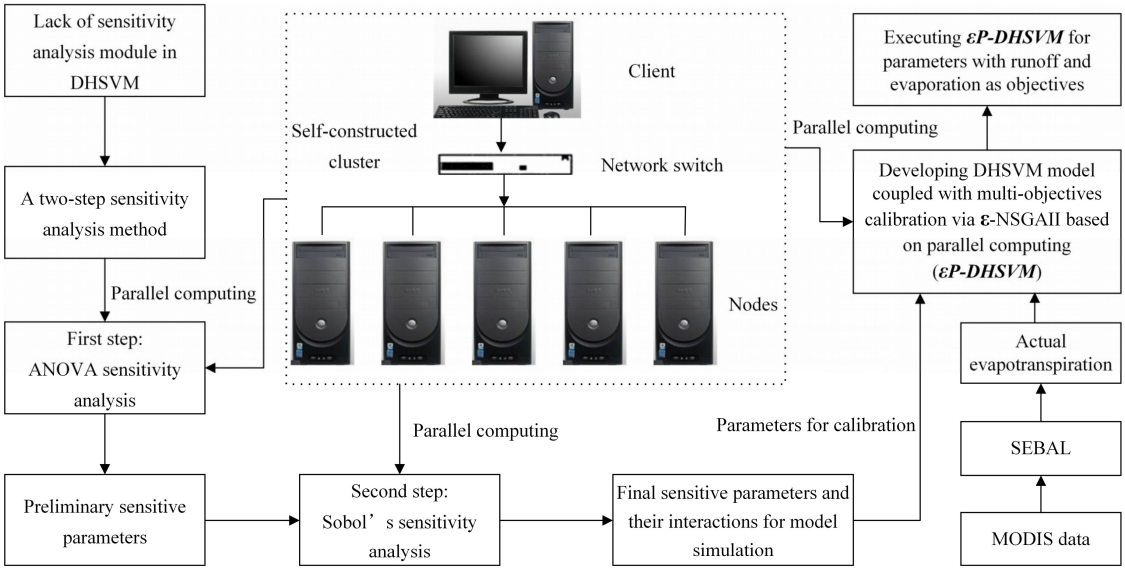


**Figure 2.** General framework used in the study.

### 3.2. Data

Five meteorological stations were used in this study, i.e., Yiwu, Dongyang, Yongkang, Jinhua and Wuyi (Figure 1b). The climate variables included daily maximum and minimum air temperature, air relative humidity, wind speed, sunshine duration and precipitation. These climate data were used to calculate potential evapotranspiration (PET) via the FAO (Food and Agriculture Organization of the United Nations) Penman-Monteith method [7,51]. The hydrological station was Jinhua Station. The period of hydro-meteorological data for model calibration was 2004–2008.

MODIS was the key instrument of Terra (originally called EOS AM-1) and Aqua (originally called EOS PM-1) satellites. Terra passes from north to south over the equator in the morning, while Aqua passes south to north across the equator in the afternoon. MODIS receive data in 36 spectral bands and the spatial resolution includes 250 m, 500 m and 1000 m. The period of MODIS data used in this study was 2004–2008, corresponding to that of hydro-meteorological data. The following MODIS Collection 3 land data products were extracted from NASA website [52]:

(a) MOD09GA: 1-day, 500 m land surface reflectance;
(b) MOD11A1: 1-day, 1-km land surface temperature;
(c) MOD13A1: 16-day, 500 m vegetation indices (NDVI).

### 3.3. SEBAL Model

SEBAL (surface energy balance algorithm for land) is a remote sensing evapotranspiration inversion model originally proposed by Bastiaanseen et al. [33], which is based on energy balance, aerodynamics and empirical relationship. This model is widely used owing to its limited data requirement and easy calculation [53]. The theoretical basis of remote sensing inversion evapotranspiration is land surface energy balance, and the equation is shown as follows:

$$R_n = G + H + \lambda \cdot ET + PH \quad (1)$$

where $R_n$ is net radiation flux, $G$ is soil heat flux, $H$ is sensible heat flux, $\lambda \cdot ET$ is latent heat flux, $\lambda$ is latent heat of vaporization, $ET$ is evapotranspiration, and $PH$ is the energy used for vegetation photosynthesis. The unit of various flux in Equation (1) is $W/m^2$.

The determination of sensible heat flux is the key to the SEBAL model, and the equation is presented as follows:

$$H = \rho \cdot C_P \cdot dT / \gamma_a \quad (2)$$

where $\rho$ is air density (kg/m$^3$), $C_P$ is the specific air heat capacity (J/kg · K), $dT$ is temperature difference between different heights ($K$), and $\gamma_a$ is Aerodynamic resistance (s/m). The calculation of sensible heat flux should be through iterative algorithms, owing to the fact that the variables $H$, $dT$ and $\gamma_a$ are all unknown and associated with each other. For the specific details of iterative algorithms and calculation of other fluxes, refer to Bastiaanseen et al. [33], Papadavid et al. [54], and Tang et al. [55].

In order to derive actual $ET$ via the SEBAL method, climate data are also needed, such as air relative humidity and solar radiation. Moreover, elevation and latitude of meteorological stations are necessary for radiation calculation.

### *3.4. DHSVM*

The distributed hydrology–soil–vegetation model (DHSVM) is a physically-based distributed hydrologic model, which provides a dynamic representation of spatial distribution of runoff, evapotranspiration, snow cover, and soil moisture at the spatial scale of digital elevation model (DEM) data [56,57]. The horizontal resolution of the DEM is typically 10–200 m. The river basin is divided into numerous computational grids based on the DEM. Soil and vegetation characteristics are allocated to each grid. The grid has hydrological connections with its adjacent neighbors through surface and subsurface flow routing. Routing surface runoff in the model has two approaches, a cell-by-cell method or a unit hydrograph method. Unsaturated moisture movement through multiple rooting zone soil layers was assessed by Darcy's law. Channel flow was routed by a cascade of liner channel reservoirs. Evapotranspiration was simulated by a two-layer canopy model, and each layer is divided into wet and dry areas. Modules related to snow were not considered in this study, due to the fact that snow is very rare in the study area. In this model, parameters included 3 categories, i.e., constant parameters, soil parameters and vegetation parameters. The constant parameter means that its value was set to a constant for the whole river basin and the entire data period used in this study, and included ground roughness and rain LAI multiplier.

The input data of the DHSVM included vegetation, soil, soil depth, stream network, the DEM and meteorological data (maximum and minimum air temperature, air relative humidity, wind speed, sunshine duration and precipitation data from 5 stations). DEM data with a resolution of 90 m were downloaded from the Shuttle Radar Topography Mission (SRTM) website (http://srtm.csi.cgiar.org/) and is redefined to 200 m due to computational burden. The vegetation and soil data were obtained from WESTDC Land Cover Products 2.0 (2006) (http://westdc.westgis.ac.cn) and Nanjing Institute of Soil Research, respectively.

This model has been widely applied to study land use change, hydrologic prediction and the effects of climate change on hydrologic processes [9,58–61].

### *3.5. Multi-Objective Calibration*

As described in Section 3.1, the final sensitivity parameters were obtained through a two-step sensitivity analysis method (first step: ANOVA sensitivity analysis, second step: Sobol's sensitivity analysis) [48]. Table 1 displays ranges, meaning, unit and abbreviation of 16 parameters of the DHSVM in Sobol's sensitivity analysis (second step) and Figure 3 shows the total order sensitivity index of these parameters. According to Tang et al. [62], a parameter is regarded as highly sensitive if its sensitivity index is larger than 0.1. Therefore, 8 parameters were highly sensitive parameters based on the total order sensitivity index shown in Figure 3, and then selected for model calibration in this study, including 1 constant parameter (rain LAI multiplier), 4 soil parameters (lateral conductivity, porosity, field capacity and wilting point of clay loam), and 3 vegetation parameters (understory monthly LAI, understory minimum resistance and root zone depths of croplands).

**Table 1.** Ranges, meaning, unit and abbreviation of 16 parameters of the DHSVM in Sobol's sensitivity analysis.

| Parameter | Meaning | Unit | Abbreviations | Range |
|---|---|---|---|---|
| Rain leaf area index (LAI) multiplier | Multiplier for LAI to determine interception capacity for rain | m | Rj | 0.00001~0.001 |
| Wilting point (L) | Wilting point for loam, used to calculate evapotranspiration | $m^3/m^3$ | θwp(L) | 0.05~0.25 |
| Lateral conductivity (CL) | Lateral saturated hydraulic conductivity for clay loam, used to calculate movement of lateral runoff | m/s | K(CL) | 0.00001~0.09 |
| Lateral conductivity exponential decrease (CL) | Exponent describing the decrease of lateral conductivity with soil depth for clay loam | / | f(CL) | 1~4 |
| Porosity (CL) | Porosity for clay loam, soil moisture content when soil is saturated | $m^3/m^3$ | φ(CL) | 0.35~0.6 |
| Field capacity (CL) | Field capacity for clay loam, used to estimate available water for subsurface layers | $m^3/m^3$ | θfc(CL) | 0.16~0.4 |
| Wilting point (CL) | Wilting point for clay loam, used to calculate evapotranspiration | $m^3/m^3$ | θwp(CL) | 0.05~0.25 |
| Bulk density (CL) | Bulk density for clay loam, used to estimate dry soil thermal conductivity | $kg/m^3$ | ρB(CL) | 1000~3000 |
| Understory height (MF) | Understory height for mixed forests | m | Uh(MF) | 0.3~2.5 |
| Overstory minimum resistance (MF) | Overstory minimum stomatal resistance for understory of mixed forests | s/m | ORsmin(MF) | 300~800 |
| Understory minimum resistance (MF) | Understory minimum stomatal resistance for mixed forests | s/m | URsmin(MF) | 50~300 |
| Understory monthly LAI (CrL) | Understory leaf area index for croplands | $m^2/m^2$ | ULAI(CrL) | 0.3~3 |
| Understory minimum resistance (CrL) | Understory minimum stomatal resistance for croplands | s/m | URsmin(CrL) | 50~300 |
| Soil moisture threshold (CrL) | Soil moisture threshold above which soil moisture does not restrict transpiration for croplands | $m^3/m^3$ | θ*(CrL) | 0.1~0.35 |
| Vapor pressure deficit (CrL) | Vapor pressure deficit threshold above which stomatal closure occurs for each vegetation layer for croplands | pa | Ec(CrL) | 1000~6000 |
| Root zone depth (CrL) | These are in effect the depths of the various soil layers for croplands | m | D(CrL) | 0.1~0.8 |

The abbreviations L, CL, MF and CrL in Table 1 represent loam and clay loam in soil types, and mixed forest and croplands in land use types, respectively.

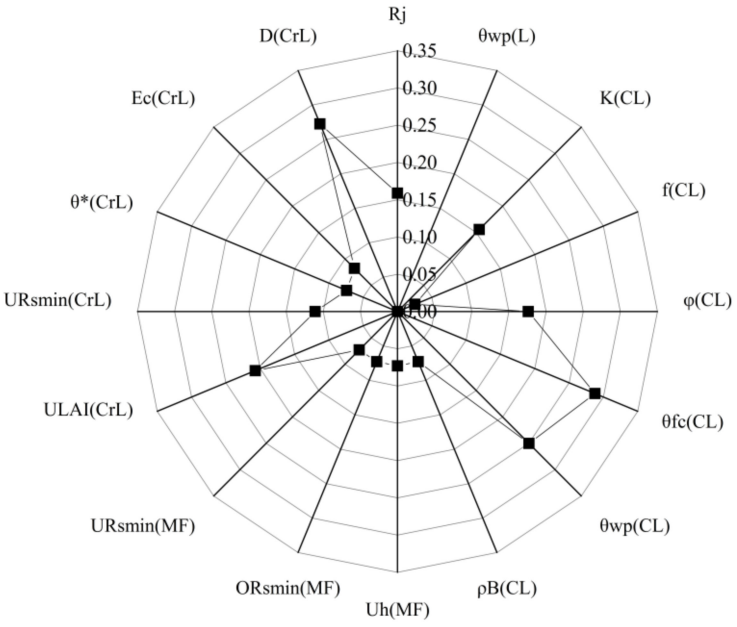


**Figure 3.** Total order sensitivity index of sixteen parameters of the DHSVM in Sobol's sensitivity analysis [48] (The abbreviations of 16 parameters are shown in Table 1).

ε-NSGAII (ε-dominance non-dominated sorted genetic algorithm II) [46] is a multi-objective evolutionary algorithm inspired by the process of natural selection. Compared with NSGAII [63], ε-NSGAII has been supplemented by ε-dominance, adaptive population sizing, and automatic termination. ε-dominance enables the user to specify the precision for each objective in a multi-objective problem. A scheme of 25% injection was used in the ε-NSGAII algorithm to direct the search. That is to say, 25% of the subsequent populations consisted of ε-non-dominance archive solutions from current populations and the other 75% were generated randomly. Automatic termination could minimize the need by terminating search based on user-specified criteria in a multi-objective problem. The application of ε-dominance, adaptive population sizing, and automatic termination make the ε-NSGAII easier to implement and could provide more reliable results than other evolutionary algorithms [64,65]. The flowchart of ε-NSGAII is showed in Figure 4.

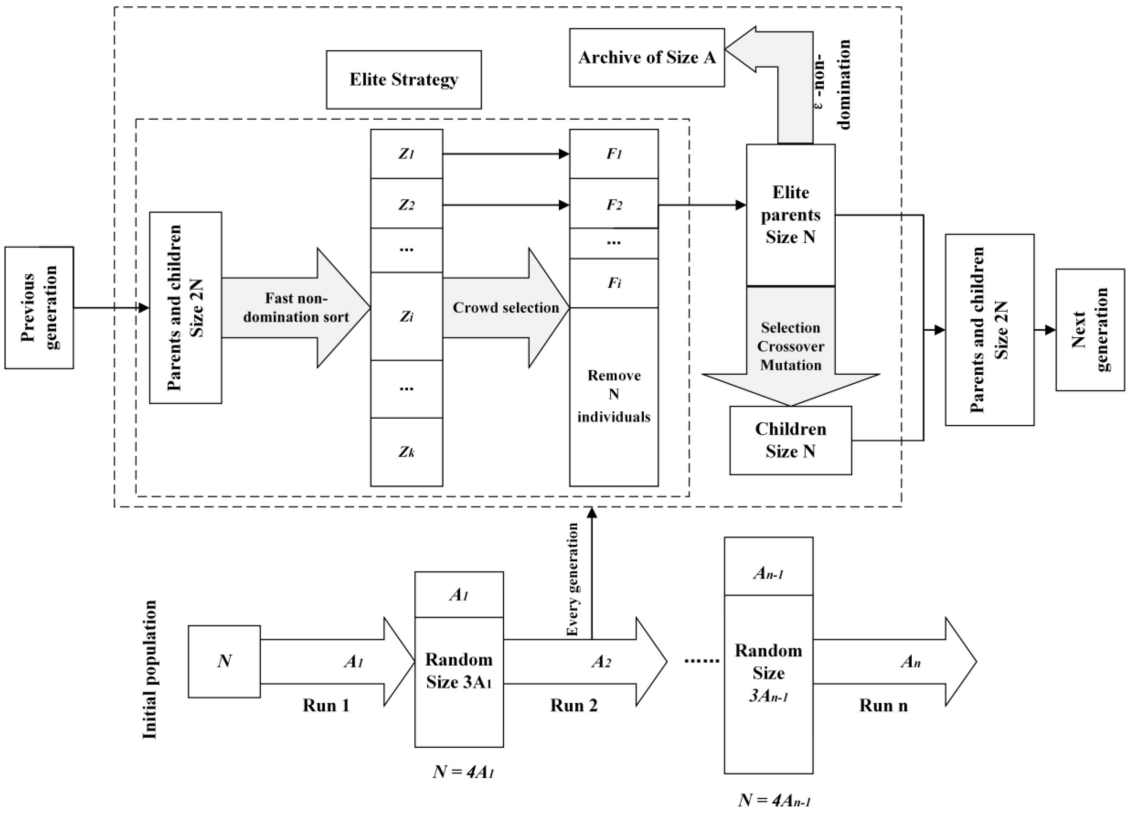


**Figure 4.** Flowchart of multi-objective calibration method ε-NSGAII (adapted from Kollat and Reed, [46]).

The selection of the objective functions (shown in Equation (5)), i.e., objectives set by users according to their demands, is very important for model calibration. In this study, Nash–Sutcliffe efficiency coefficient (*NS*) and model estimation bias in the percentage (*PBIAS*) of runoff and evapotranspiration were chosen as objective functions. The Nash–Sutcliffe efficiency determines the relative difference of residual variance compared with the observation variance [66]. *PBIAS* could ensure the water balance in model simulation. The equations for *NS* and *PBIAS* are presented as follows:

$$NS = 1 - \frac{\sum_{i=1}^{n} (O_i - S_i)^2}{\sum_{i=1}^{n} (O_i - \bar{O})^2} \quad (3)$$

$$PBIAS(\%) = abs\left(\frac{100 \times \sum_{i=1}^{n}(S_i - O_i)}{\sum_{i=1}^{n}(O_i)}\right) \quad (4)$$

where $O_i$ represents observed runoff, $S_i$ represents simulated runoff, and $\overline{O}$ represents the average of observed runoff.

The multi-objective calibration of the DHSVM can be described as follows:

$$\text{Minimize}\{1 - NS_E,\ PBIAS_E,\ 1 - NS_R,\ PBIAS_R\} \quad (5)$$

where $NS_E$ refers to $NS$ for evapotranspiration; $PBIAS_E$ refers to $PBIAS$ for evapotranspiration; $NS_R$ refers to $NS$ for runoff; and $PBIAS_R$ refers to $PBIAS$ for runoff.

Due to high computation demands of the DHSVM and large sample requirements in sensitivity analyses and model calibration, parallel computing is applied in this study. A self-constructed cluster consisting of five personal computers with the same configuration was used. The logistical setup of the cluster was a master–slave distribution (i.e., one processor set as master and the other processors set as slaves). In model calibration, multiple model runs were in parallel with a message passing interface (MPI) program. In each generation, the master allocated individuals equally to slaves, and gathered objective values from slaves after they are evaluated. The next generation was then determined based on the rules of ε-NSGAII, including elite strategy, selection, crossover and mutation.

## 4. Results

### *4.1. Time Series of Remote Sensing Evapotranspiration*

Time series of MODIS evapotranspiration on a daily time scale are obtained through the SEBAL model. Owing to the lack of actual evapotranspiration observation in the study area, potential evapotranspiration (PET) calculated by the FAO Penman-Monteith method is used to examine the accuracy of MODIS-ET [39,41,67]. Figure 5 presents the comparison of monthly areal MODIS-ET and PET time series of Jinhua River Basin. From this figure, it can be observed that MODIS-ET shows reasonable performance. Overall, MODIS-ET is lower than PET, which is rational, owing to the fact that PET is the quantification of evapotranspiration ability with sufficient moisture, i.e., the maximum of actual evapotranspiration. The correlation coefficients between MODIS-ET and PET on daily and monthly time scales are 0.89 and 0.94, respectively.

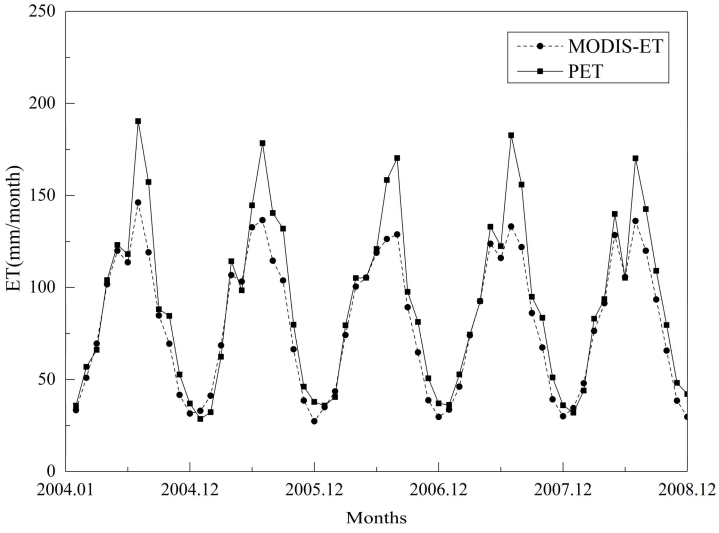


**Figure 5.** Monthly areal moderate resolution imaging spectrometer- evapotranspiration (MODIS-ET) and potential evapotranspiration (PET) time series of Jinhua River Basin.

### *4.2. Single Objective Model Calibration Results*

Figure 6 shows the solution distribution of objective space from single objective calibration (only runoff is used as calibration objective). In order to present a better search process, only ranges (0–1 for *NS* and 0.0006–60% for *PBIAS*) are shown in Figure 6. From this figure, it can be observed that some relationship may exist between *NS* and *PBIAS*. Hence, a function is found to fit the relationship between them and its fitting effect is quite reasonable, as shown in Figure 6. The bottom left corner represents the optimal solution, i.e., the values for *NS* is 1.0 and for *PBIAS* is 0. The smaller the distance between the solution and the bottom left corner, the better the performance of the runoff simulation. From the solution distribution, it is found that the maximum value of *NS* is 0.79 and minimum value of *PBIAS* is 0.0006%, but the optimal solution does not exist (i.e., where the best values of two objective functions occur in one solution). To analyze the performance of runoff simulation, a tradeoff solution, which makes compromises between the two objective functions, is shown as R1 (minimum value of sum of distance's square to the optimal point, i.e., *NS* is 1.0 and *PBIAS* is 0) in Figure 6.

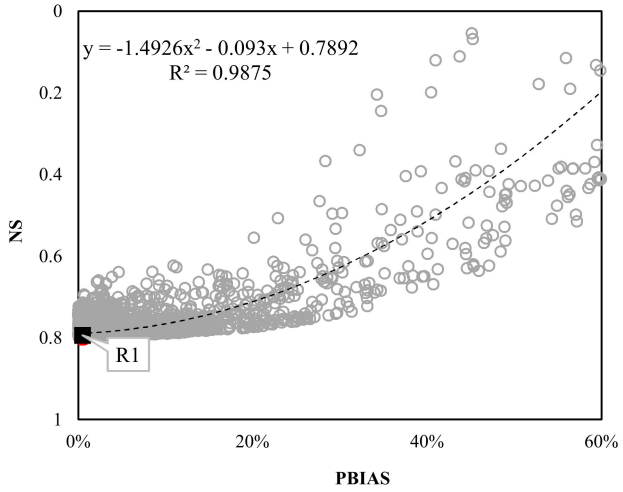


**Figure 6.** Solution distribution in objective space of Nash–Sutcliffe efficiency coefficient (*NS*) and percentage estimation bias (*PBIAS*) of runoff obtained by single objective calibration.

The comparison between observed and simulated runoff for solution R1 is shown in Figure 7a. The *NS* and *PBIAS* for R1 are 0.79 and −0.5%, respectively. Table 2 shows the evaluation standard of hydrological indices for the performance of the model simulation [59]. According to Table 2, the performance of runoff simulation is very good overall. From Figure 7a, it can be observed that peak flows are to some extent underestimated. Possible reasons for this include that: (1) preferential flow is not considered in the DHSVM; (2) there is the assumption that the understory or bare soil covers the entire cell in evapotranspiration module; and (3) meteorological data on a daily instead of an hourly time scale is used. Similar conclusions are obtained by Kelleher et al. [68] and Kuraś et al. [69], who found the underestimation of peak flow in hydrologic simulation using the DHSVM.

The comparison of simulated monthly areal actual ET and MODIS-ET for R1 is shown in Figure 7b. It is obvious that the performance of evapotranspiration simulation is not very good. Underestimation of actual ET is very common, especially in summer. The *NS* and *PBIAS* for actual ET on a daily time scale are 0.14% and −30.8%, respectively. On a monthly time scale, the *NS* value is 0.25. Therefore, it can be concluded that the good performance of runoff simulation could not guarantee the performance of other hydrologic elements, for example, actual evapotranspiration, in this study. This conclusion is consistent with that of [70], who calibrated the HBV rainfall–runoff model with a single objective, either runoff or evapotranspiration, and found that the other output variable was poorly simulated in both cases.

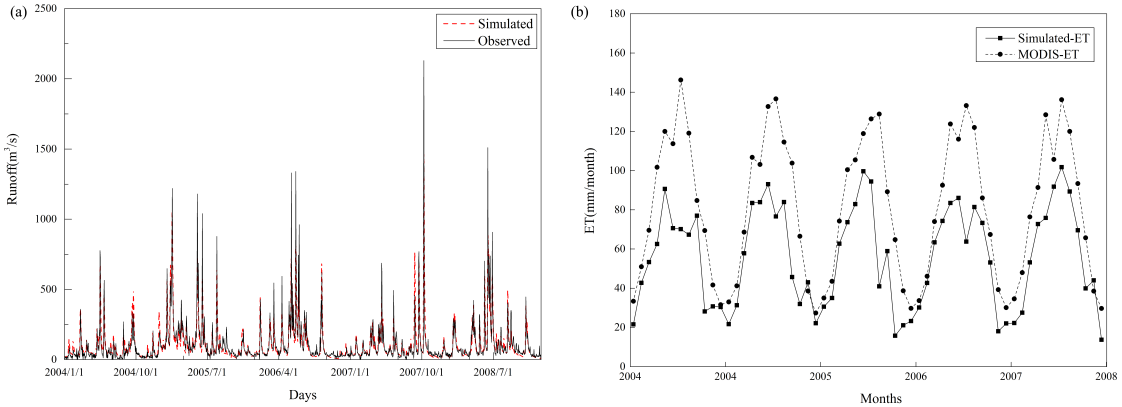


**Figure 7.** (**a**) Comparison of daily observed and simulated runoff and (**b**) comparison of simulated monthly areal evapotranspiration and MODIS-ET for R1 solution from single objective calibration.

**Table 2.** Evaluation standard of hydrological indices for performance of model simulation [59].

| *PBIAS* (%) | $15\% < PBIAS < 25\%$ average performance | $10\% \leq PBIAS \leq 15\%$ good | $PBIAS < 10\%$ very good |
|---|---|---|---|
| *NS* | $0.35 < NS < 0.5$ average performance | $0.5 \leq NS \leq 0.7$ good | $0.7 < NS$ very good |
| $R^2$ | $0.49 < R^2 \leq 0.64$ average performance | $0.64 < R^2 \leq 0.81$ good | $R^2 > 0.81$ very good |

### *4.3. Multi-Objective Calibration Results*

Results of multi-objective calibration are obtained through εP-DHSVM, with both runoff and evapotranspiration as objectives (i.e., *NS* of runoff and evapotranspiration and *PBIAS* of runoff and evapotranspiration). The self-developed εP-DHSVM model with parallel computing algorithm is able to conduct multi-objective calibration efficiently and effectively, with its calculation speed improved by more than 20 times. Figure 8 shows the solution distribution in objective space of *NS* (Figure 8a) and *PBIAS* (Figure 8b) of runoff and evapotranspiration. Figure 9 presents the solution distribution in objective space between *NS* and *PBIAS* for runoff (Figure 9a) and evapotranspiration (Figure 9b). Similarly, functions are found to describe the relationship between $NS_R/NS_E$ and $PBIAS_R/PBIAS_E$ and their fitting effect is very good. In order to clearly analyze the simulation performance of runoff and evapotranspiration in multi-objective calibration, three tradeoff solutions (R, E and RE) are selected and shown in Figures 8 and 9. Solutions R and E are derived by making compromises between two objective functions of runoff and evapotranspiration, respectively. Solution RE is obtained by making compromises among four objective functions of runoff and evapotranspiration.

Figure 10 shows the daily observed and simulated runoff for solution R. The *NS* efficiency coefficient and *PBIAS* for R are 0.79 and −1.6%, respectively. Compared with solution R1 in the single objective calibration (shown in Section 4.2), the model performance of runoff simulation by solution R is slightly improved.

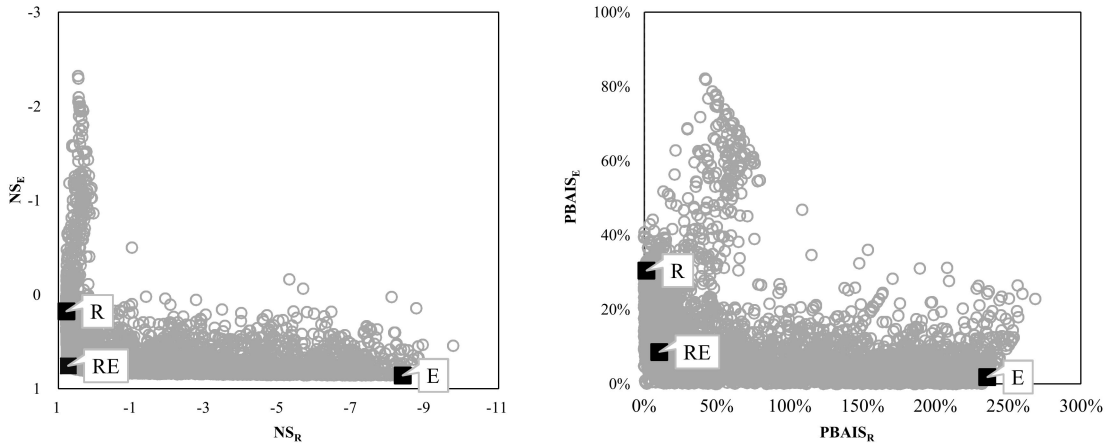


(**a**) (**b**)

**Figure 8.** (**a**) Solution distribution in objective space of *NS* of runoff and evapotranspiration, and (**b**) in objective space of *PBIAS* of runoff and evapotranspiration from multi-objective calibration for runoff and evapotranspiration.

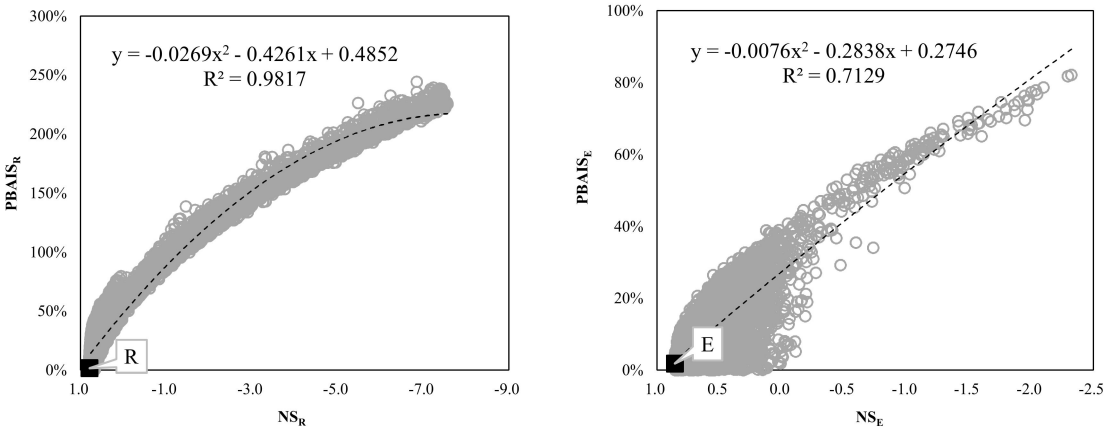


(**a**) (**b**)

**Figure 9.** (**a**) Solution distribution in objective space of *NS* and *PBIAS* of runoff, and (**b**) in objective space of *NS* and *PBIAS* of evapotranspiration from multi-objective calibration for runoff and evapotranspiration.

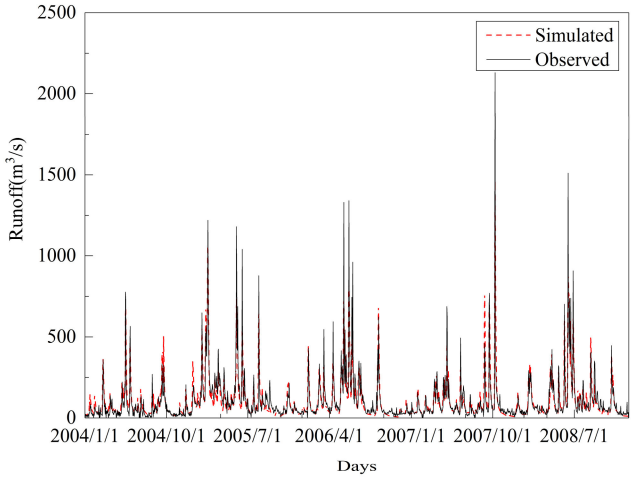


**Figure 10.** Comparison of daily observed and simulated runoff for solution R from multi-objective calibration.

Figure 11a presents the monthly areal simulated ET and MODIS-ET for solution E. As shown in this figure, the simulation of evapotranspiration by the DHSVM is very reasonable. The *NS* and *PBIAS* for daily evapotranspiration are 0.86 and −1.9%, respectively. On a monthly time scale, the *NS* value is 0.95. According to Table 2, the performance is very good. *PBAIS* between the simulated ET and MODIS-ET on a monthly time scale for solution E are presented in Figure 11b. The range of *PBIAS* is −13.2–19.9%, within the acceptable range (−25–25%). Except for a few months (September, November and December), evapotranspiration is underestimated. The *PBIAS* values are various for different months. The maximum value is 19.9% for November and the minimum value is −0.2% for October.

The model performance of runoff and evapotranspiration for solutions R and E were analyzed, respectively, above. As shown in Figure 8, two efficiency values of evapotranspiration for R, and runoff for E, are not good.

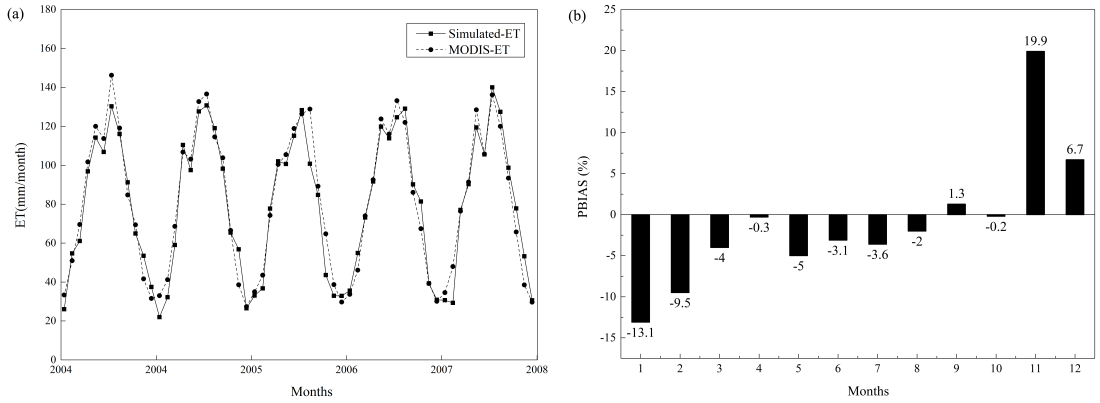


**Figure 11.** (**a**) Comparison of monthly areal simulated ET and MODIS-ET, and (**b**) *PBAIS* between simulated-ET and MODIS-ET for solution E from multi-objective calibration.

For solution RE based on four objective functions, the $NS_R$ and $PBIAS_R$ values are 0.74 and −10% on a daily time scale, respectively. On a monthly time scale, the $NS_R$ value is 0.89. This shows a very satisfactory performance of runoff simulation by solution RE. In addition, the simulation of evapotranspiration is also satisfactory, based on the comparison of simulated evapotranspiration and MODIS-ET shown in Figure 12b. On a daily time scale, the values are 0.76 and −8.6% for $NS_E$ and $PBIAS_E$ respectively. On a monthly time scale, the $NS_E$ value is 0.86. According to Table 2, solution RE shows very good model performance for runoff and evapotranspiration in this study area.

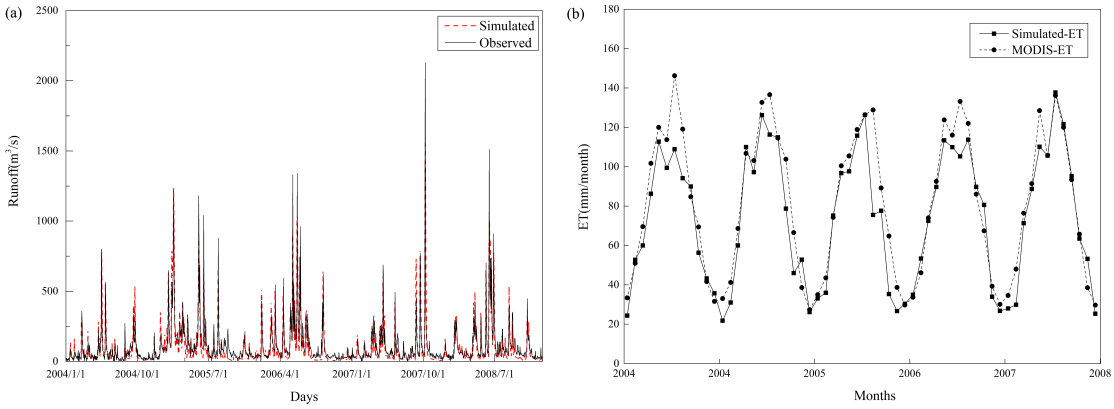


**Figure 12.** (**a**) Comparison of daily observed and simulated runoff, and (**b**) comparison of monthly areal simulated-ET and MODIS-ET for solution RE from multi-objective calibration.

## 5. Discussion

In this study, the DHSVM was calibrated for the Jinhua River Basin using observed runoff and remote sensing evapotranspiration obtained from MODIS via the SEBAL method. In order

to illustrate whether the equifinality problem is improved in multi-objective calibration, Table 3 shows values of eight calibrated parameters for trade-off solutions (R1, R, E, RE) from single and multiple objective calibrations. For solution R1, the DHSVM performs well for runoff modelling and simulates evapotranspiration poorly. As shown in Table 3, the value of understory LAI of croplands is much smaller than the other three trade-off solutions (R, E, RE). A small value of LAI will result in underestimation of actual evapotranspiration, owing to the fact that LAI has a great impact on the capacity of canopy interception and acquisition of solar radiation. Moreover, vegetation minimum resistance affects vegetation transpiration. A high value of lateral conductivity speeds up lateral flow movement, which may lead to decrease of soil evaporation. The vegetation parameters are completely concentrated in croplands, which may be owing to its maximum percentage (55.4%) in the study area. This leads to vegetation parameters of croplands playing larger roles than other for land use types.

For single objective calibration, high equifinality occurred, due to the broader parameter ranges for good performance ($NS > 0.7$ and $PBIAS < 10\%$) of runoff simulation. For porosity of clay loam, the range is 0.4–0.6 $m^3/m^3$. The narrower the parameter range, the lower the equifinality or uncertainty. For multi-objective calibration, the parameter ranges of good performance ($NS_R > 0.7$, $NS_E > 0.7$, $PBIAS_R < 10\%$ and $PBIAS_E < 10\%$) are much lower than for single objective calibration, such as 0.55–0.59 $m^3/m^3$ for porosity of clay loam. Therefore, multi-objective calibration can, to a great extent, mitigate the problem of equifinality, which is in line with the work of Rajib et al. [5] and Wanders et al. [71]. The results of these studies confirmed the strong effect of remote sensing data in reducing equifinality when integrated into multi-objective calibration. Moreover, reducing the number of calibration parameters [72] or adding more observations can also address the equifinality issue to some extent [73]. In addition, the increasing applications of remote sensing data in hydrological modeling has the potential to mitigate the equifinality problem [74].

**Table 3.** Specific values of eight calibrated parameters for trade-off solutions from single and multi-objective calibration (R1, R, E, RE).

| Parameters | R1 | R | E | RE |
|---|---|---|---|---|
| Rj | 0.0007 | 0.0004 | 0.0003 | 0.0003 |
| K(CL) | 0.02620 | 0.00008 | 0.00013 | 0.00012 |
| φ(CL) | 0.60 | 0.59 | 0.58 | 0.59 |
| θfc(CL) | 0.34 | 0.36 | 0.38 | 0.39 |
| θwp(CL) | 0.05 | 0.06 | 0.05 | 0.06 |
| ULAI(CrL) | 0.38 | 0.98 | 1.52 | 1.11 |
| URsmin(CrL) | 174 | 206 | 216 | 209 |
| D(CrL) | 0.02 | 0.17 | 0.17 | 0.17 |

Runoff and evapotranspiration are two major outputs of hydrological models. Changes in one will influence the other. Therefore, the accuracy of evapotranspiration acts in an important role in achieving reasonable simulation of runoff. For remote sensing data, its accuracy varies greatly owing to heterogeneity of land surface and variation of climate [75]. As a result, solely MODIS-derived actual evapotranspiration data (MOD16 ET) may not be able to capture landscape heterogeneity [76]. Yang et al. [75] compared three remote sensing ET models with observations and revealed that two energy balance-based models perform much better in terms of accuracy of deriving evapotranspiration than the MOD16 ET model. In this study, the accuracy of remote sensing ET obtained through the SEBAL method coupled with MODIS products and meteorological variables, such as air relative humidity [55], can be further enhanced, resulting in better accuracy. Nevertheless, how to verify the accuracy in remote sensing ET is still a crucial issue. In this study, PET estimated by FAO Penman-Monteith is used as a benchmark to check the accuracy of remote sensing evapotranspiration derived from MODIS via the SEBAL model. However, PET refers to the maximum potential of evapotranspiration under adequate water supply [7] while remote sensing evapotranspiration refers to actual evapotranspiration instead of potential evapotranspiration. Hence, PET and remote sensing evapotranspiration are different. In fact, observation data of actual evapotranspiration is very rare.

Observation equipment used to measure actual evapotranspiration is usually in the form of evaporation pans, including Φ 20 cm, Φ 80 cm, E601 and class A pans [9,77,78]. As is known, evaporation pans have adequate water when used to measure actual evapotranspiration. This is more similar to PET but is still not actual evapotranspiration. One frequently used approach to solve this issue is isotope measurement [79–84]. The advantage of isotope measurement is its accuracy, while the disadvantages are that it is time-consuming and not suitable for large-scale problems. Remote sensing data is indeed an effective resource to obtain actual evapotranspiration for large-scale problems. The models or methods applied to derive actual evapotranspiration from remote sensing data should be improved and developed in the future [75,85,86].

This study can provide useful insights for hydrological modeling, in particular for regions where data are scare. More studies should follow to explore the effect of different remote sensing products for hydrological modeling and other fields.

## 6. Conclusions

This study integrated remote sensing evapotranspiration into multi-objective calibration of a fully distributed hydrological model (DHSVM) in a humid region in east China. The remote sensing evapotranspiration was derived from MODIS through the SEBAL model. Moreover, this study developed a multi-objective calibration module based on parallel computing of a Linux cluster for the DHSVM (εP-DHSVM) and applied it to Jinhua River Basin. Eight sensitivity parameters, obtained from a two-step sensitivity analysis approach, were used in model calibration, including single objective calibration and multi-objective calibration. In single objective calibration, runoff was the only objective and two objective functions ($NS_R$ and $PBIAS_R$) of runoff were adopted. In multi-objective calibration, remote sensing evapotranspiration was integrated. Two objectives, including runoff and evapotranspiration, and four objective functions ($NS_R$, $PBIAS_R$, $NS_E$, and $PBIAS_E$) were used. The following conclusions can be drawn:

1. Compared with potential evapotranspiration, MODIS-ET estimated by SEBAL showed a satisfactory performance, with high values of efficiency coefficients on daily (0.89) and monthly (0.94) time scales, which illustrates the accuracy of MODIS-ET in the Jinhua River Basin.
2. Runoff was simulated reasonably in single objective calibration with an *NS* value of 0.79 and a *PBIAS* value of 0.5%, whereas evapotranspiration was not. High equifinality occurred in single objective calibration.
3. The multi-objective calibration by integrating remote sensing evapotranspiration showed good performance for runoff and evapotranspiration simulation with reasonable value of objective functions ($NS_R$: 0.74, $PBIAS_R$: −10%, $NS_E$: 0.76 and $PBIAS_E$: −8.6%). Furthermore, multi-objective calibration to a great extent alleviated the problem of equifinality.
4. The self-developed model, εP-DHSVM, can implement multi-objective calibration effectively and efficiently, with its calculation speed improved more than 20 times.

**Author Contributions:** Conceptualization, Y.-P.X.; Methodology, S.P. and L.L.; Software, S.P. and Z.B.; Validation, S.P., L.L. and Z.B.; Formal Analysis, S.P., L.L. and Z.B.; Investigation, S.P.; Resources, Y.-P.X.; Data Curation, S.P.; Writing-Original Draft Preparation, S.P.; Writing-Review & Editing, Y.-P.X.; Visualization, S.P., L.L. and Z.B.; Supervision, Y.-P.X.; Project Administration, Y.-P.X.; Funding Acquisition, Y.-P.X.

**Funding:** The work here is financially supported by National Key Research and Development Plan "Inter-governmental Cooperation in International Scientific and Technological Innovation" (2016YFE0122100), National Natural Science Foundation of China (91547106) and Zhejiang Provincial Natural Science Foundation of China (LR14E090001).

**Acknowledgments:** National Climate Center of China Meteorological Administration and Zhejiang Hydrological Bureau are greatly acknowledged for providing hydrological and meteorological data used in this study.

**Conflicts of Interest:** The authors declare no conflicts of interest.

## References


1. Gupta, H.V.; Sorooshian, S.; Yapo, P.O. Toward improved calibration of hydrologic models: Multiple and non-commensurable measures of information. *Water Resour. Res.* **1998**, *34*, 751–763. [CrossRef]
2. Henriksen, H.J.; Troldborg, L.; Nyegaard, P.; Sonnenborg, T.O.; Refsgaard, J.C.; Madsen, B. Methodology for construction, calibration and validation of a national hydrological model for Denmark. *J. Hydrol.* **2003**, *280*, 52–71. [CrossRef]
3. Immerzeel, W.W.; Droogers, P. Calibration of a distributed hydrological model based on satellite evapotranspiration. *J. Hydrol.* **2008**, *349*, 411–424. [CrossRef]
4. Abbaspour, K.C.; Rouholahnejad, E.; Vaghefi, S.; Srinivasan, R.; Yang, H.; Klove, B. A continental-scale hydrology and water quality model for Europe: Calibration and uncertainty of a high-resolution large-scale SWAT model. *J. Hydrol.* **2015**, *524*, 733–752. [CrossRef]
5. Rajib, M.A.; Merwade, V.; Yu, Z. Multi-objective calibration of a hydrologic model using spatially distributed remotely sensed/in-situ soil moisture. *J. Hydrol.* **2016**, *536*, 192–207. [CrossRef]
6. Daggupati, P.; Yen, H.; White, M.J.; Srinivasan, R.; Arnold, J.G.; Keitzer, C.S.; Sowa, S.P. Impact of model development, calibration and validation decisions on hydrological simulations in West Lake Erie Basin. *Hydrol. Process.* **2015**, *29*, 5307–5320. [CrossRef]
7. Xu, Y.; Pan, S.; Fu, G.; Tian, Y.; Zhang, X. Future potential evapotranspiration changes and contribution analysis in Zhejiang Province, East China. *J. Geophys. Res. Atmos.* **2014**, *119*, 2174–2192. [CrossRef]
8. Xie, H.; Zhu, X.; Yuan, D. Pan evaporation modelling and changing attribution analysis on the Tibetan Plateau (1970–2012). *Hydrol. Process.* **2015**, *29*, 2164–2177. [CrossRef]
9. Xu, Y.; Pan, S.; Gao, C.; Fu, G.; Chiang, Y. Historical pan evaporation changes in the Qiantang River Basin, East China. *Int. J. Climatol.* **2016**, *36*, 1928–1942. [CrossRef]
10. Chen, H.; Chandrasekar, V. The quantitative precipitation estimation system for Dallas-Fort Worth (DFW) urban remote sensing network. *J. Hydrol.* **2015**, *531*, 259–271. [CrossRef]
11. Cheng, G.; Han, J.; Guo, L.; Liu, Z.; Bu, S.; Ren, J. Effective and Efficient Midlevel Visual Elements-Oriented Land-Use Classification Using VHR Remote Sensing Images. *IEEE Trans. Geosci. Remote Sens.* **2015**, *53*, 4238–4249. [CrossRef]
12. Chew, C.; Shah, R.; Zuffada, C.; Hajj, G.; Masters, D.; Mannucci, A.J. Demonstrating soil moisture remote sensing with observations from the UK TechDemoSat-1 satellite mission. *Geophys. Res. Lett.* **2016**, *43*, 3317–3324. [CrossRef]
13. Kussul, N.; Lavreniuk, M.; Skakun, S.; Shelestov, A. Deep Learning Classification of Land Cover and Crop Types Using Remote Sensing Data. *IEEE Geosci. Remote Sens. Lett.* **2017**, *14*, 778–782. [CrossRef]
14. Parajuli, P.B.; Jayakody, P.; Ouyang, Y. Evaluation of Using Remote Sensing Evapotranspiration Data in SWAT. *Water Resour. Manag.* **2018**, *32*, 985–996. [CrossRef]
15. Sadeghi, M.; Jones, S.B.; Philpot, W.D. A linear physically-based model for remote sensing of soil moisture using short wave infrared bands. *Remote Sens. Environ.* **2015**, *164*, 66–76. [CrossRef]
16. Zeng, J.; Li, Z.; Chen, Q.; Bi, H.; Qiu, J.; Zou, P. Evaluation of remotely sensed and reanalysis soil moisture products over the Tibetan Plateau using in-situ observations. *Remote Sens. Environ.* **2015**, *163*, 91–110. [CrossRef]
17. Zhang, Y.Q.; Chiew, F.H.S.; Zhang, L.; Leuning, R.; Cleugh, H.A. Estimating catchment evaporation and runoff using MODIS leaf area index and the Penman-Monteith equation. *Water Resour. Res.* **2008**, *44*. [CrossRef]
18. Birkinshaw, S.J.; Moore, P.; Kilsby, C.G.; O'Donnell, G.M.; Hardy, A.J.; Berry, P.A.M. Daily discharge estimation at ungauged river sites using remote sensing. *Hydrol. Process.* **2014**, *28*, 1043–1054. [CrossRef]
19. Faridzad, M.; Yang, T.; Hsu, K.; Sorooshian, S.; Xiao, C. Rainfall frequency analysis for ungauged regions using remotely sensed precipitation information. *J. Hydrol.* **2018**, *563*, 123–142. [CrossRef]
20. Marra, F.; Morin, E.; Peleg, N.; Mei, Y.; Anagnostou, E.N. Intensity-duration-frequency curves from remote sensing rainfall estimates: Comparing satellite and weather radar over the eastern Mediterranean. *Hydrol. Earth Syst. Sci.* **2017**, *29*, 2389–2404. [CrossRef]
21. Poortinga, A.; Bastiaanssen, W.; Simons, G.; Saah, D.; Senay, G.; Fenn, M.; Bean, B.; Kadyszewski, J. A Self-Calibrating Runoff and Streamflow Remote Sensing Model for Ungauged Basins Using Open-Access Earth Observation Data. *Remote Sens.* **2017**, *9*, 86. [CrossRef]
22. Rhee, J.; Im, J. Meteorological drought forecasting for ungauged areas based on machine learning: Using long-range climate forecast and remote sensing data. *Agric. For. Meteorol.* **2017**, *237*, 105–122. [CrossRef]

23. Sun, W.C.; Ishidaira, H.; Bastola, S. Towards improving river discharge estimation in ungauged basins: Calibration of rainfall-runoff models based on satellite observations of river flow width at basin outlet. *Hydrol. Earth Syst. Sci.* **2010**, *14*, 2011–2022. [CrossRef]
24. Alton, P.B. Retrieval of seasonal Rubisco-limited photosynthetic capacity at global FLUXNET sites from hyperspectral satellite remote sensing: Impact on carbon modelling. *Agric. For. Meteorol.* **2017**, *232*, 74–88. [CrossRef]
25. Gao, H.; Birkett, C.; Lettenmaier, D.P. Global monitoring of large reservoir storage from satellite remote sensing. *Water Resour. Res.* **2012**, *48*. [CrossRef]
26. Hu, L.; Li, W.; Xu, B. The role of remote sensing on studying mangrove forest extent change. *Int. J. Remote Sens.* **2018**, *39*, 6440–6462. [CrossRef]
27. Khan, S.I.; Hong, Y.; Wang, J.; Yilmaz, K.K.; Gourley, J.J.; Adler, R.F.; Brakenridge, G.R.; Policelli, F.; Habib, S.; Irwin, D. Satellite Remote Sensing and Hydrologic Modeling for Flood Inundation Mapping in Lake Victoria Basin: Implications for Hydrologic Prediction in Ungauged Basins. *IEEE Trans. Geosci. Remote Sens.* **2011**, *49*, 85–95. [CrossRef]
28. Park, H.; Kim, Y.; Kimball, J.S. Widespread permafrost vulnerability and soil active layer increases over the high northern latitudes inferred from satellite remote sensing and process model assessments. *Remote Sens. Environ.* **2016**, *175*, 349–358. [CrossRef]
29. Richardson, A.D.; Hufkens, K.; Milliman, T.; Frolking, S. Intercomparison of phenological transition dates derived from the PhenoCam Dataset V1.0 and MODIS satellite remote sensing. *Sci. Rep.* **2018**, *8*, 5679. [CrossRef]
30. Yang, J.; Gong, P.; Fu, R.; Zhang, M.; Chen, J.; Liang, S.; Xu, B.; Shi, J.; Dickinson, R. The role of satellite remote sensing in climate change studies. *Nat. Clim. Chang.* **2013**, *3*, 875–883. [CrossRef]
31. Bhattarai, N.; Shaw, S.B.; Quackenbush, L.J.; Im, J.; Niraula, R. Evaluating five remote sensing based single-source surface energy balance models for estimating daily evapotranspiration in a humid subtropical climate. *Int. J. Appl. Earth Obs.* **2016**, *49*, 75–86. [CrossRef]
32. Su, Z. The Surface Energy Balance System (SEBS) for estimation of turbulent heat fluxes. *Hydrol. Earth Syst. Sci.* **2002**, *6*, 85–100. [CrossRef]
33. Bastiaanssen, W.; Menenti, M.; Feddes, R.A.; Holtslag, A. A remote sensing surface energy balance algorithm for land (SEBAL)-1. Formulation. *J. Hydrol.* **1998**, *212*, 198–212. [CrossRef]
34. Anderson, M.C.; Norman, J.M.; Diak, G.R.; Kustas, W.P.; Mecikalski, J.R. A two-source time-integrated model for estimating surface fluxes using thermal infrared remote sensing. *Remote Sens. Environ.* **1997**, *60*, 195–216. [CrossRef]
35. Kustas, W.P.; Norman, J.M. Evaluation of soil and vegetation heat flux predictions using a simple two-source model with radiometric temperatures for partial canopy cover. *Agric. For. Meteorol.* **1999**, *94*, 13–29. [CrossRef]
36. Norman, J.M.; Kustas, W.P.; Humes, K.S. Source approach for estimating soil and vegetation energy fluxes in observations of directional radiometric surface temperature. *Agric. For. Meteorol.* **1995**, *77*, 263–293. [CrossRef]
37. Allen, R.G.; Tasumi, M.; Trezza, R. Satellite-based energy balance for mapping evapotranspiration with internalized calibration (METRIC)-Model. *J. Irrig. Drain. Eng.* **2007**, *133*, 380–394. [CrossRef]
38. Li, Z.; Tang, R.; Wan, Z.; Bi, Y.; Zhou, C.; Tang, B.; Yan, G.; Zhang, X. A Review of Current Methodologies for Regional Evapotranspiration Estimation from Remotely Sensed Data. *Sensors* **2009**, *9*, 3801–3853. [CrossRef]
39. Bastiaanssen, W.; Noordman, E.; Pelgrum, H.; Davids, G.; Thoreson, B.P.; Allen, R.G. SEBAL model with remotely sensed data to improve water-resources management under actual field conditions. *J. Irrig. Drain. Eng.* **2005**, *131*, 85–93. [CrossRef]
40. Jaber, H.S.; Mansor, S.; Pradhan, B.; Ahmad, N. Evaluation of SEBAL model for Evapotranspiration mapping in Iraq using remote sensing and GIS. *Int. J. Appl. Eng. Res.* **2016**, *11*, 3950–3955.
41. Kalma, J.D.; McVicar, T.R.; McCabe, M.F. Estimating Land Surface Evaporation: A Review of Methods Using Remotely Sensed Surface Temperature Data. *Surv. Geophys.* **2008**, *29*, 421–469. [CrossRef]
42. Bouda, M.; Rousseau, A.N.; Gumiere, S.J.; Gagnon, P.; Konan, B.; Moussa, R. Implementation of an automatic calibration procedure for HYDROTEL based on prior OAT sensitivity and complementary identifiability analysis. *Hydrol. Process.* **2014**, *28*, 3947–3961. [CrossRef]
43. Goldberg, D.E. *Genetic Algorithms in Search, Optimization, and Machine Learning*; Addison Wesley: Boston, MA, USA, 1989.
44. Holland, J.H. *Adaptation in Natural and Artificial Systems*; University of Michigan Press: Ann Arbor, MI, USA, 1975.

45. Kollat, J.B.; Reed, P.M. The value of online adaptive search: A performance comparison of NSGAII, ε-NSGAII and εMOEA. In Proceedings of the International Conference on Evolutionary Multi-Criterion Optimization, Guanajuato, Mexico, 9–11 March 2005; pp. 386–398.
46. Kollat, J.B.; Reed, P.M. Comparing state-of-the-art evolutionary multi-objective algorithms for long-term groundwater monitoring design. *Adv. Water Resour.* **2006**, *29*, 792–807. [CrossRef]
47. Du, E.; Link, T.E.; Gravelle, J.A.; Hubbart, J.A. Validation and sensitivity test of the distributed hydrology soil-vegetation model (DHSVM) in a forested mountain watershed. *Hydrol. Process.* **2014**, *28*, 6196–6210. [CrossRef]
48. Pan, S.; Fu, G.; Chiang, Y.; Ran, Q.; Xu, Y. A two-step sensitivity analysis for hydrological signatures in Jinhua River Basin, East China. *Hydrol. Sci. J.* **2017**, *62*, 2511–2530. [CrossRef]
49. Saltelli, A.; Chan, K.; Scott, E.M. *Sensitivity Analysis*; Wiley: Hoboken, NJ, USA, 2000.
50. Sobol, I.M. Global sensitivity indices for nonlinear mathematical models and their Monte Carlo estimates. *Math. Comput. Simul.* **2001**, *55*, 271–280. [CrossRef]
51. Allen, R.G. An update for the calculation of potential evapotranspiration. *ICID Bull.* **1994**, *43*, 35–92.
52. Ran, Y.; Li, X.; Lu, L. Evaluation of four remote sensing based land cover products over China. *Int. J. Remote Sens.* **2010**, *31*, 391–401. [CrossRef]
53. Paul, G.; Gowda, P.H.; Prasad, P.V.V.; Howell, T.A.; Aiken, R.M.; Neale, C.M.U. Investigating the influence of roughness length for heat transport (z(oh)) on the performance of SEBAL in semi-arid irrigated and dryland agricultural systems. *J. Hydrol.* **2014**, *509*, 231–244. [CrossRef]
54. Papadavid, G.; Hadjimitsis, D.G.; Toulios, L.; Michaelides, S. A Modified SEBAL Modeling Approach for Estimating Crop Evapotranspiration in Semi-arid Conditions. *Water Resour. Manag.* **2013**, *27*, 3493–3506. [CrossRef]
55. Tang, R.; Li, Z.; Chen, K.; Jia, Y.; Li, C.; Sun, X. Spatial-scale effect on the SEBAL model for evapotranspiration estimation using remote sensing data. *Agric. For. Meteorol.* **2013**, *174*, 28–42. [CrossRef]
56. Wigmosta, M.S.; Nijssen, B.; Storck, P.; Lettenmaier, D.P. The distributed hydrology soil vegetation model. *Math. Model. Small Watershed Hydrol. Appl.* **2002**, *43*, 7–42.
57. Wigmosta, M.S.; Vail, L.W.; Lettenmaier, D.P. A distributed hydrology-vegetation model for complex terrain. *Water Resour. Res.* **1994**, *30*, 1665–1679. [CrossRef]
58. Jost, G.; Moore, R.D.; Weiler, M.; Gluns, D.R.; Alila, Y. Use of distributed snow measurements to test and improve a snowmelt model for predicting the effect of forest clear-cutting. *J. Hydrol.* **2009**, *376*, 94–106. [CrossRef]
59. Safeeq, M.; Fares, A. Hydrologic response of a Hawaiian watershed to future climate change scenarios. *Hydrol. Process.* **2012**, *26*, 2745–2764. [CrossRef]
60. Sun, N.; Yearsley, J.; Baptiste, M.; Cao, Q.; Lettenmaier, D.P.; Nijssen, B. A spatially distributed model for assessment of the effects of changing land use and climate on urban stream quality. *Hydrol. Process.* **2016**, *30*, 4779–4798. [CrossRef]
61. Sun, N.; Yearsley, J.; Voisin, N.; Lettenmaier, D.P. A spatially distributed model for the assessment of land use impacts on stream temperature in small urban watersheds. *Hydrol. Process.* **2015**, *29*, 2331–2345. [CrossRef]
62. Tang, Y.; Reed, P.; Wagener, T.; Van Werkhoven, K. Comparing sensitivity analysis methods to advance lumped watershed model identification and evaluation. *Hydrol. Earth Syst. Sci. Discuss.* **2007**, *11*, 793–817. [CrossRef]
63. Deb, K.; Pratap, A.; Agarwal, S.; Meyarivan, T. A fast and elitist multiobjective genetic algorithm: NSGA-II. *IEEE Trans. Evol. Comput.* **2002**, *6*, 182–197. [CrossRef]
64. Ferringer, M.P.; Spencer, D.B.; Reed, P. Many-objective Reconfiguration of Operational Satellite Constellations with the Large-Cluster Epsilon Non-dominated Sorting Genetic Algorithm-II. In Proceedings of the 2009 IEEE Congress on Evolutionary Computation, Trondheim, Norway, 18–21 May 2009; p. 340.
65. Reed, P.M.; Hadka, D.; Herman, J.D.; Kasprzyk, J.R.; Kollat, J.B. Evolutionary multiobjective optimization in water resources: The past, present, and future. *Adv. Water Resour.* **2013**, *51*, 438–456. [CrossRef]
66. Nash, J.E.; Sutcliffe, J.V. River flow forecasting through conceptual models. Part 1. A discussion of principles. *J. Hydrol.* **1970**, *10*, 282–290. [CrossRef]
67. Wu, B.F.; Shao, J.H. Temporal and spatial extension of evaportranspiration estimated from remote sensing. *J. Hydraul. Eng.* **2006**, *37*, 286–292.

68. Kelleher, C.; McGlynn, B.; Wagener, T. Characterizing and reducing equifinality by constraining a distributed catchment model with regional signatures, local observations, and process understanding. *Hydrol. Earth Syst. Sci.* **2017**, *21*, 3325–3352. [CrossRef]
69. Kuras, P.K.; Alila, Y.; Weiler, M.; Spittlehouse, D.; Winkler, R. Internal catchment process simulation in a snow-dominated basin: Performance evaluation with spatiotemporally variable runoff generation and groundwater dynamics. *Hydrol. Process.* **2011**, *25*, 3187–3203. [CrossRef]
70. Rientjes, T.H.M.; Muthuwatta, L.P.; Bos, M.G.; Booij, M.J.; Bhatti, H.A. Multi-variable calibration of a semi-distributed hydrological model using streamflow data and satellite-based evapotranspiration. *J. Hydrol.* **2013**, *505*, 276–290. [CrossRef]
71. Wanders, N.; Bierkens, M.F.P.; de Jong, S.M.; de Roo, A.; Karssenberg, D. The benefits of using remotely sensed soil moisture in parameter identification of large-scale hydrological models. *Water Resour. Res.* **2014**, *50*, 6874–6891. [CrossRef]
72. Fu, C.; James, A.L.; Yao, H. Investigations of uncertainty in SWAT hydrologic simulations: A case study of a Canadian Shield catchment. *Hydrol. Process.* **2015**, *29*, 4000–4017. [CrossRef]
73. Qiao, L.; Pan, Z.; Herrmann, R.B.; Hong, Y. Hydrological variability and uncertainty of lower missouri river basin under changing climate. *J. Am. Water Resour. Assoc.* **2014**, *50*, 246–260. [CrossRef]
74. Lettenmaier, D.P.; Alsdorf, D.; Dozier, J.; Huffman, G.J.; Pan, M.; Wood, E.F. Inroads of remote sensing into hydrologic science during the WRR era. *Water Resour. Res.* **2015**, *51*, 7309–7342. [CrossRef]
75. Yang, Y.; Long, D.; Guan, H.; Liang, W.; Simmons, C.; Batelaan, O. Comparison of three dual-source remote sensing evapotranspiration models during the MUSOEXE-12 campaign: Revisit of model physics. *Water Resour. Res.* **2015**, *51*, 3145–3165. [CrossRef]
76. Mu, Q.; Zhao, M.; Running, S.W. Improvements to a MODIS global terrestrial evapotranspiration algorithm. *Remote Sens. Environ.* **2011**, *115*, 1781–1800. [CrossRef]
77. Fu, G.B.; Liu, C.M.; Chen, S.L.; Hong, E.L. Investigating the conversion coefficients for free water surface evaporation of different evaporation pans. *Hydrol. Process.* **2004**, *18*, 2247–2262. [CrossRef]
78. Lim, W.H.; Roderick, M.L.; Hobbins, M.T.; Wong, S.C.; Farquhar, G.D. The energy balance of a US Class A evaporation pan. *Agric. For. Meteorol.* **2013**, *182*, 314–331. [CrossRef]
79. Good, S.P.; Soderberg, K.; Guan, K.; King, E.G.; Scanlon, T.M.; Caylor, K.K. 2H isotopic flux partitioning of evapotranspiration over a grass field following a water pulse and subsequent dry down. *Water Resour. Res.* **2014**, *50*, 1410–1432. [CrossRef]
80. Hu, Z.; Wen, X.; Sun, X.; Li, L.; Yu, G.; Lee, X.; Li, S. Partitioning of evapotranspiration through oxygen isotopic measurements of water pools and fluxes in a temperate grassland. *J. Geophys. Res. Biogeosci.* **2014**, *119*, 358–371. [CrossRef]
81. Ma, Y.; Song, X. Applying stable isotopes to determine seasonal variability in evapotranspiration partitioning of winter wheat for optimizing agricultural management practices. *Sci. Total Environ.* **2018**, *654*, 633–642. [CrossRef] [PubMed]
82. Wei, Z.; Yoshimura, K.; Okazaki, A.; Kim, W.; Liu, Z.; Yokoi, M. Partitioning of evapotranspiration using high-frequency water vapor isotopic measurement over a rice paddy field. *Water Resour. Res.* **2015**, *51*, 3716–3729. [CrossRef]
83. Wen, X.; Yang, B.; Sun, X.; Lee, X. Evapotranspiration partitioning through in-situ oxygen isotope measurements in an oasis cropland. *Agric. For. Meteorol.* **2016**, *230*, 89–96. [CrossRef]
84. Xiao, W.; Wei, Z.; Wen, X. Evapotranspiration partitioning at the ecosystem scale using the stable isotope method-A review. *Agric. For. Meteorol.* **2018**, *263*, 346–361. [CrossRef]
85. Liou, Y.; Kar, S.K. Evapotranspiration Estimation with Remote Sensing and Various Surface Energy Balance Algorithms—A Review. *Energies* **2014**, *7*, 2821–2849. [CrossRef]
86. Nouri, H.; Glenn, E.P.; Beecham, S.; Boroujeni, S.C.; Sutton, P.; Alaghmand, S.; Noori, B.; Nagler, P. Comparing Three Approaches of Evapotranspiration Estimation in Mixed Urban Vegetation: Field-Based, Remote Sensing-Based and Observational-Based Methods. *Remote Sens.* **2016**, *8*, 492. [CrossRef]